# Electric Polarization from a Many-Body Neural Network Ansatz

Xiang Li,[1,*,†] Yubing Qian,[1,2,*] and Ji Chen[2,3,‡]
[1]ByteDance Research, Zhonghang Plaza, No. 43, North 3rd Ring West Road, Haidian District, Beijing, People's Republic of China
[2]School of Physics, Peking University, Beijing 100871, People's Republic of China
[3]Interdisciplinary Institute of Light-Element Quantum Materials, Frontiers Science Center for Nano-Optoelectronics, Peking University, Beijing 100871, People's Republic of China

(Received 15 August 2023; revised 1 December 2023; accepted 22 March 2024; published 25 April 2024)

*Ab initio* calculation of dielectric response with high-accuracy electronic structure methods is a long-standing problem, for which mean-field approaches are widely used and electron correlations are mostly treated via approximated functionals. Here we employ a neural network wave function ansatz combined with quantum Monte Carlo method to incorporate correlations into polarization calculations. On a variety of systems, including isolated atoms, one-dimensional chains, two-dimensional slabs, and three-dimensional cubes, the calculated results outperform conventional density functional theory and are consistent with the most accurate calculations and experimental data. Furthermore, we have studied the out-of-plane dielectric constant of bilayer graphene using our method and reestablished its thickness dependence. Overall, this approach provides a powerful tool to accurately describe electron correlation in the modern theory of polarization.

DOI: 10.1103/PhysRevLett.132.176401

Electric polarization plays a crucial role in electromagnetic phenomena such as ferro- and piezoelectricity. Despite its significance, a proper microscopic definition of polarization was only formulated in the 1990s [1,2], which revealed the hidden relation between physical polarization and the Berry phase of solid systems. This theoretical advance leads to successful calculations of the dielectric response of solid materials from first principles [3–5], which is critical in several fields of condensed matter physics, such as the ferroelectric and topological materials [6]. However, the underlying electronic structure methods are mostly mean-field approaches, such as density functional theory (DFT) [7], which has its limitation because the result depends heavily on the so-called exchange-correlation functional. Exchange-correlation functionals cannot fully account for the exact correlation effects of electrons. In particular, widely used semilocal functionals often produce an excessive overestimate of electric susceptibility [5,8]. Although correlated wave function methods, such as coupled-cluster theory, can also be employed to calculate polarization [9], their high computational complexity hinders their application in solid systems. Furthermore, most of these correlated electronic structure methods are limited in open boundary condition (OBC) for polarization calculations, which leads to slow convergence and heavy computational costs toward the thermodynamic limit (TDL); see Fig. 1 for a summary of the state-of-the-art methods in polarization calculations.

In addition to the conventional deterministic electronic structure methods mentioned above, quantum Monte Carlo (QMC) methods are also widely adopted for electronic structure calculations, showing favorable computational scaling and high accuracy [10–12]. Pioneering works to study electric susceptibility using QMC methods have been reported [13,14], in which a traditional Slater-Jastrow-type wave function is combined with diffusion Monte Carlo (DMC) method to study polarization of hydrogen chains in periodic boundary condition (PBC). The main difficulty for DMC method is to write down the local self-consistent Hamiltonian under a finite electric field and run calculations iteratively. Despite the promising results on hydrogen chains [13], there are still grand challenges: multiple loops of DMC simulation are needed for the self-consistent

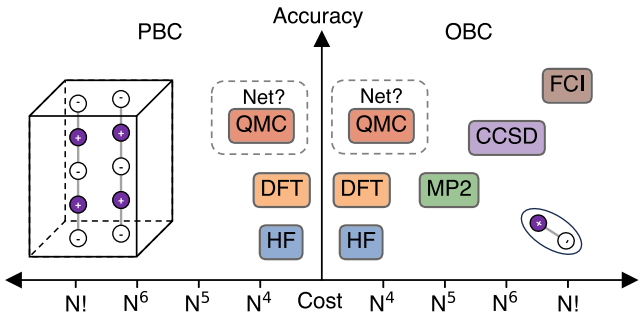


FIG. 1. A brief illustration of the computational cost and accuracy of different electronic structure methods in polarization calculations. $N$ denotes the number of electrons in the system. High-level correlated wave function methods are not shown in the PBC panel because they have not been applied to PBC polarization calculations so far. MP2, second-order Møller-Plesset perturbation theory; CCSD, coupled cluster with single and double excitations; FCI, full configuration interaction.

 

procedure, a complex forward walking strategy is required for evaluating the polarization, and the quality of trial wave function affects the accuracy of DMC method. Therefore, it is desirable to develop more accurate and efficient approaches to calculate the electric polarization of solid systems.

In recent years, there has been significant progress in the application of neural networks in the electronic structure community. Neural network wave function ansatz combined with QMC simulations has demonstrated higher accuracy with lower computational complexity [$\mathcal{O}(N^4)$] than conventional high-order wave function methods [15–33]. The expressiveness of neural networks overcomes the main bottleneck of traditional wave function ansatz in QMC method, making the approach a competitive option for state-of-the-art electronic structure calculation. So far, the neural network QMC calculations have shown great power in treating spin systems [15–17], molecules [18–21], periodic models [25–28], and real solids [28,29].

In this Letter, we extend the neural network QMC calculation to the electric polarization of solid systems. Specifically, we employ a recently developed solid neural network, dubbed DeepSolid (DS) [28], in conjunction with variational Monte Carlo methods. Antithetic sampling [34] is employed for efficient computation of the Berry phase and thus the electric polarization. We test our approach on a diverse range of systems, including isolated atoms, one-dimensional chains, two-dimensional slabs, three-dimensional cubes, and bilayer graphene. The results demonstrate the accuracy of our approach over traditional methods.

To introduce our methodology, let us consider a crystal system under a finite electric field $\mathbf{E}$; the enthalpy of this system is formulated below [3,4,13,35],

$$F[\psi] = \frac{\langle\psi|\hat{H}_S|\psi\rangle}{\langle\psi|\psi\rangle} - \Omega_S \mathbf{E}\cdot\mathbf{P}[\psi], \tag{1}$$

where $\hat{H}_S$ denotes the supercell Hamiltonian in the absence of electric field $\mathbf{E}$, and $\Omega_S$ is the supercell volume. The term $-\Omega_S\mathbf{E}\cdot\mathbf{P}$ represents the interaction between electric polarization density $\mathbf{P}$ and electric field. However, a proper microscopic definition of $\mathbf{P}[\psi]$ remained absent for decades since the ordinary position operator $\hat{\mathbf{r}}$ violates the periodic boundary condition. This problem was finally solved after recognizing the polarization as the Berry phase in the Brillouin zone, according to which the polarization can be extracted from a general wave function $\psi$ as follows [36]:

$$\mathbf{P}[\psi] = -\frac{1}{\Omega_S}\sum_i \frac{\mathbf{a}_i}{2\pi}\mathrm{Im}\ln\frac{\langle\psi|\hat{U}_i|\psi\rangle}{\langle\psi|\psi\rangle},$$
$$\hat{U}_i = \exp\left[i\mathbf{b}_i\cdot\left(\sum_e \hat{\mathbf{r}}_e - \sum_I Z_I\mathbf{R}_I\right)\right], \tag{2}$$

where $\mathbf{a}_i$, $\mathbf{b}_i$ denote lattice and reciprocal lattice vectors of the supercell. $\hat{U}_i$ serves as a periodic generalization of the position operator $\hat{\mathbf{r}}$ in solid systems and $\mathrm{Im}\ln(x)$ is used to extract the Berry phase within $x$. Note that $\hat{U}_i$ is an intrinsic many-body operator that includes all the electron coordinates in the exponent. A charge-weighted sum of ion coordinates $Z_I\mathbf{R}_I$ is also included to achieve translation invariance of polarization.

With the enthalpy functional formulated above, traditional methods usually start with a Hartree-Fock (HF) ansatz, which is typically expressed as follows:

$$\psi_{\mathrm{HF}}(\mathbf{r}) = \mathrm{Det}[e^{i\mathbf{k}_i\cdot\mathbf{r}_j}u_{\mathbf{k}_i}(\mathbf{r}_j)]. \tag{3}$$

Electrons are treated independent of each other with a mean-field interaction in Eq. (3), simplifying quantum many-body problems, but also deviating from the ground truth. To fully treat the electron correlation effects, we employ a correlated neural network wave function $\psi_{\mathrm{net}}$ from DeepSolid [28], whose general form reads

$$\psi_{\mathrm{net}}(\mathbf{r}) = \mathrm{Det}[e^{i\mathbf{k}_i\cdot\mathbf{r}_j}u_{\mathbf{k}_i}(\mathbf{r}_j;\mathbf{r}_{\neq j})], \tag{4}$$

where $\mathbf{r}_{\neq j}$ denotes all the electron coordinates except $\mathbf{r}_j$. Equation (4) resembles the form of the traditional Bloch function, while cell-periodic functions $u_{\mathbf{k}}$ are now represented using deep neural networks that rely on all electrons to accommodate electron correlations [19]. Electron features $\mathbf{r}_i$ are converted to be periodic and permutation equivariant before being fed into neural networks, and complex-valued orbitals $u_{\mathbf{k}}$ are constructed with a pair of neural networks outputting the real and imaginary part, respectively. As a result, Fermionic antisymmetry, periodicity, and complex-valued nature are all encoded in our network, promoting it to be a legitimate and expressive ansatz for solids. See Ref. [28] for more details of the architecture.

Using the neural network we have constructed, the enthalpy functional outlined in Eq. (1) can be efficiently minimized through variational Monte Carlo method, allowing for gradual convergence to the ground truth. However, the polarization estimator in Eq. (2) has a large variance, and a direct evaluation will seriously impede optimization. As a solution, antithetic sampling is employed in the Monte Carlo evaluation, which reads

$$\langle\hat{U}_i\rangle = \frac{\int d\mathbf{r}|\psi(\mathbf{r})|^2 U_i(\mathbf{r})}{\int d\mathbf{r}|\psi(\mathbf{r})|^2} = \frac{\int d\mathbf{r}|\psi(\mathbf{r})|^2 \tilde{U}_i(\mathbf{r})}{\int d\mathbf{r}|\psi(\mathbf{r})|^2},$$
$$\tilde{U}_i(\mathbf{r}) = \frac{1}{2}\left[U_i(\mathbf{r}) + \frac{|\psi(-\mathbf{r})|^2}{|\psi(\mathbf{r})|^2}U_i(-\mathbf{r})\right]. \tag{5}$$

Thus, the fluctuations are significantly reduced through the cancellation between $U_i(\mathbf{r})$ and its inverted image $U_i(-\mathbf{r})$. A more detailed discussion of the polarization estimator in QMC method is included in Supplemental Material [37]. It is worth noting that centrosymmetric cells are assumed in

TABLE I. Calculated atom polarizability in atomic units (bohr$^3$). B3LYP, HF, and CCSD(T) results are calculated with PySCF [44] in the def2-qzvppd basis set and nonrelativistic limit. Parameters and training curves of DeepSolid are presented in Supplemental Material, Sec. V [37]. Recommended data are taken from Ref. [45], which is deduced from experiment data and the most accurate calculations.

| | H | He | Li | Be | N | Ne | MAE |
|---|---|---|---|---|---|---|---|
| B3LYP | 5.187 | 1.485 | 142.727 | 43.090 | 7.711 | 2.838 | 4.669 |
| HF | 4.484 | 1.318 | 169.231 | 45.441 | 7.138 | 2.365 | 2.243 |
| CCSD(T) | 4.484 | 1.372 | 165.803 | **37.707** | **7.212** | 2.642 | 0.326 |
| DS | **4.511**(**1**) | **1.3903**(**3**) | **165.0**(**1**) | 36.95(2) | 7.16(1) | **2.672**(**4**) | 0.32 |
| Recommended | 4.5(exact) | 1.38375(2) | 164.1125(5) | 37.74(3) | 7.4(2) | 2.66110(3) | 0 |

Eq. (5), and one can choose other images for cancellation if central symmetry is not satisfied. To further improve efficiency, we have employed a Kronecker-factored curvature estimator optimizer [38], which effectively integrates second-order information into the optimization process, surpassing traditional optimizers. See Supplemental Material [37] for more computational details, including recommended hyperparameters.

Isolated atoms are the first systems selected for direct comparison with the most accurate methods and experimental data. In our calculations, we place a single atom in a large enough box to eliminate periodic image interactions and the electric field is tuned small enough to ignore high-order contributions [39–42]. The calculated polarizability $\alpha$ is shown in Table I, which measures the linear response of the dipole moment to the applied field and has some subtle relation with the bulk susceptibility $\chi$ (Supplemental Material, Sec. III [37]). Results from DFT with the Becke's gradient-corrected hybrid exchange-correlation density functional, HF, and CCSD(T) under OBC are also listed for comparison. *P*-state atoms (B, C, O, F) are skipped because their anisotropy requires special treatments [43]. As can be seen from Table I, although B3LYP is a widely trusted functional belonging to the fourth rung of the so-called Jacob's ladder of DFT, it consistently deviates from the ground truth and has a relatively large mean absolute error (MAE). The behavior of DFT is due to the inaccuracy in treating the exchange-correlation effects, which can be very different for energy and polarization calculations. In HF calculations, because of the explicit treatment of nonlocal exchange, deviations in polarization are significantly reduced. CCSD(T) is the coupled-cluster theory with single, double, and perturbative triple excitations and is considered a very accurate method in the literature. It further incorporates correlation effects on top of HF wave functions and achieves smaller MAE than HF results. Overall, DeepSolid results are comparable with CCSD(T), showing that the exchange-correlation treatments in our neural network are accurate and reliable for polarization calculations.

Having demonstrated our technique with single atoms, we proceed to simulate periodic systems by arranging bonded molecules into a one-dimensional chain and a two-dimensional slab. These systems are widely known as challenging cases for conventional DFT methods, which would have a serious overestimation of their longitudinal susceptibility. This problem stems from the fact that surface charges are insensitive to the bulk charge within the system when nonlocal interactions are absent, and this can be solved using more accurate *ab initio* methods [5]. For the one-dimensional case, hydrogen chain ($nH_2$) and polyyne ($nC_2$) are studied, and the simulation size is pushed to 22 $H_2$ and 9 $C_2$, respectively, for TDL convergence. Correlation-consistent effective core potential is employed for polyyne to accelerate neural network optimization and reduce fluctuation [31,46]. The final results are plotted in Fig. 2, which show that susceptibility calculated by DeepSolid agrees well with correlated wave function methods CCSD(T) and random phase approximation

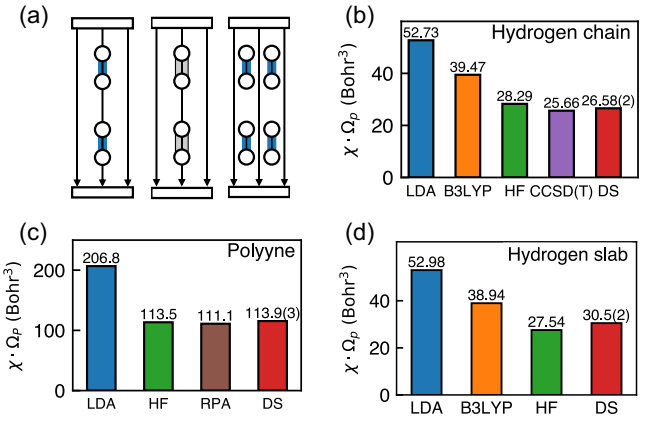


FIG. 2. Calculations of chains and slabs. (a) Illustrations of hydrogen chain, polyyne, hydrogen slab, and the applied electric field. (b) Hydrogen chain, (c) Polyyne, (d) Hydrogen slab susceptibilities $\chi$. $\Omega_p$ denotes the volume of the primitive cell. Parameters and training curves of DeepSolid are presented in Supplemental Material, Secs. VI–VIII [37]. For the hydrogen system, LDA and HF results were calculated with the 3–21G basis set under PBC [5]. CCSD(T) calculations were performed with the 6–311G$^{**}$ basis set under OBC [9]. Intra- and interpair distances are set to 2 and 3 bohr, respectively, for the hydrogen chain. The interchain distance is set to 4.724 bohr for the slab. For polyyne, the alternating distance between carbon atoms is set to 1.18 and 1.4 Å. LDA, HF, and RPA results were calculated with 6–31G, 3–21G, and 4–31G basis sets, respectively, under OBC [49–51].

(RPA). Local-density approximation (LDA) functional deviates severely from the ground truth for one-dimensional chains [9], but the use of hybrid functions such as B3LYP leads to partial recovery of nonlocal exchange effects and, consequently, a reduction in the overshot. HF is much better than DFT calculations, which further proves the importance of the nonlocal exchange effect for electric polarization calculation in this system. As we arrange hydrogen chains periodically to form hydrogen slabs, the computational cost of high-level deterministic wave function methods, such as CCSD(T), grows rapidly and is soon beyond reach. However, our approach has a lower scaling and enables us to extend the simulation size to the $6 \times 6$ supercell. Additional HF calculations are performed using the Vienna *ab initio* simulation package (VASP) code [47,48], which further prove the convergence of our simulation (Supplemental Material, Sec. VII [37]). Based on this, we obtain the first accurate polarization calculation for such a hydrogen slab. For the slab, the performances of DFT and HF compared with our accurate neural network results are similar to those observed for the chains.

To further test our method, we applied it to alkali metal hydrides and calculated their dielectric constants, allowing direct comparison with experimental results. These systems have a simple structure, consisting of alternating cations and anions, but they are of considerable research significance due to their relevance in hydrogen storage applications [52]. The high-frequency dielectric constant $\epsilon_\infty$ can be extracted through optical experiments from the following relations:

$$\begin{aligned} \mathbf{D} &= \epsilon_\infty \mathbf{E} = \mathbf{E} + 4\pi \mathbf{P}, \\ \epsilon_\infty &= 1 + 4\pi\chi = n_{\mathrm{D}}^2, \end{aligned} \tag{6}$$

where $n_{\mathrm{D}}$ denotes the corresponding refractive index. In the visible light regime, ions are almost frozen relative to the incident light frequency and this leads to the dominance of electric polarization in $\epsilon_\infty$. It is worth noting that three-dimensional systems are qualitatively different from chains and slabs. Specifically, for a $d$-dimensional supercell with intrinsic length $L$ in all directions, the fluctuation of the $\hat{U}_i$ exponent is proportional to $L^{d-2}$, which means that the fluctuation increases at large $L$ for three-dimensional systems (Supplemental Material, Sec. I [37]). To balance the influence from finite-size error and $\hat{U}_i$ fluctuations, we only tile the conventional cell in the direction of the applied electric field $\mathbf{E}$. Moreover, the Burkatzki-Filippi-Dolg pseudopotential [53] is used to further reduce the cost by removing inertial core electrons [31]. The final results reported in Fig. 3 employ a $4 \times 1 \times 1$ supercell with a $1 \times 3 \times 3$ twist average, which ensures convergence to the thermodynamic limit within a small range. Extended discussions on the finite-size error and details of twist average are presented in Supplemental Material, Sec. IX [37]. In Fig. 3, LDA, Perdew-Burke-Ernzerhof (PBE) and HF results

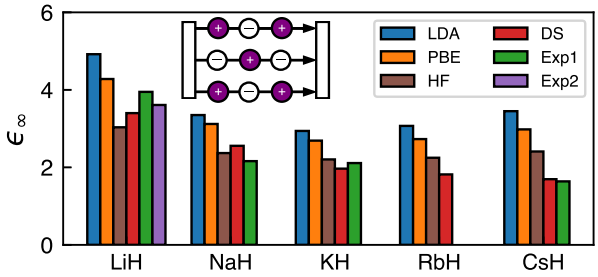


FIG. 3. Calculated high-frequency dielectric constant $\epsilon_\infty$ of alkali metal hydrides XH. Statistical errors are negligible for the presented data. LDA and PBE results in PBC are taken from Ref. [55]. HF results are obtained using the VASP code. Experimental data are taken from Refs. [56–58]. Exp1 is derived from the refractive indexes $n_{\mathrm{D}}$ for sodium doublet (589.29 nm) via Eq. (6), and Exp2 is the extrapolated result toward infinite wave length. RbH experiments are absent.

are also plotted for comparison, while more accurate conventional wave function methods are not applicable due to computational costs. As we can see, numerical simulations and experiments agree that $\epsilon_\infty$ decreases as the alkali metal atom becomes heavy, since $\epsilon_\infty$ is inversely proportional to the cell volume in Eq. (6). However, LDA and PBE functionals [54] tend to overestimate $\epsilon_\infty$, and the error is largest in CsH. In contrast, our DeepSolid results agree well with the experiment for all systems, which manifest the capability of neural network wave functions to capture nonlocal exchange and correlation effects.

After demonstrating the accuracy of our methods in previous sections, we now proceed to apply our method to bilayer graphene (BLG), an extensively studied two-dimensional material system known for its rich electronic properties. Despite its fundamental importance, the precise value of the dielectric constant of BLG remains elusive and has been an important subject of both experimental and theoretical works [59,60]. Specifically, theoretical calculations reported were either restricted to DFT level [59] or based on values calculated with monolayer graphene [60]. Here we use DeepSolid to directly calculate the out-of-plane dielectric constant $\epsilon_\infty^\perp$ of bilayer graphene. $2 \times 2$ supercells containing monolayer and equilibrium AA-stacked bilayer graphene were used (see Supplemental Material, Secs. VII X and XI [37] for details on twist average and finite-size errors). The calculated monolayer polarizability equals $5.7(1)$ bohr$^3$ and bilayer polarizability equals $11.6(1)$ bohr$^3$, which agrees with the linear dependence of polarizability on the number of layers as shown in Ref. [59]. Based on this linear dependence and following Ref. [61], one can derive the expression of the out-of-plane dielectric constant as a function of the layer separation $d$ (see Supplemental Material, Sec. III [37]),

$$\epsilon_\infty^\perp(d) = \left(1 - \frac{2\pi\alpha_{\mathrm{equil}}^{\mathrm{BLG}}}{Sd}\right)^{-1}, \tag{7}$$

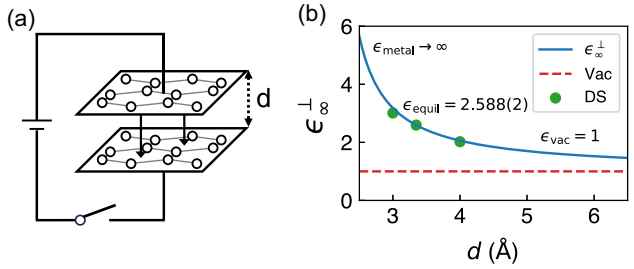


FIG. 4. Calculated effective two-dimensional dielectric constant $\epsilon_\infty^\perp$ of bilayer graphene. Statistical errors are negligible for the presented data. (a) Bilayer graphene under electric field. (b) Calculated $\epsilon_\infty^\perp$ as a function of graphene layer distance $d$. The equilibrium separation of BLG is set to 3.347 Å.

where $S = 5.25$ Å$^2$ denotes the area of the primitive cell. Using the computed polarizability $\alpha_{\text{equil}}^{\text{BLG}}$, we can reestablish the relation of $\epsilon_\infty^\perp$, which is plotted in Fig. 4. To further check Eq. (7), we also calculate the polarizability of bilayer graphene at slightly larger (4 Å) and smaller (3 Å) layer distances and plot the corresponding dielectric constant in Fig. 4, and the results agree well with each other. Moreover, there are two notable limits when varying the layer separation $d$: as $d$ decreases, two graphene layers coincide with each other and the system becomes metallic, which explains the diverging of $\epsilon_\infty^\perp$; as $d$ becomes large, BLG polarization becomes negligible and vacuum contribution dominates in $\epsilon_\infty^\perp$ which approaches unity. The thickness-dependent dielectric constant will be valuable for further understanding and tuning the stacked multilayer graphene systems.

In conclusion, this work proposes an accurate method for investigating solid polarization based on the recently developed solid neural network wave function combined with quantum Monte Carlo method. For a large range of systems, the errors of our calculations are one order of magnitude smaller than the workhorse methods such as DFT. The absolute errors in susceptibility are on the order of 0.1 bohr$^3$ and the relative errors are within a few percent, whereas the uncertainty of DFT calculations may be larger than 50%. Our approach provides a reliable solution to the electric polarization in solids with explicit treatment of many-body electron correlation effects. The accurate polarization data can also be used to evaluate the performance of newly developed DFT functionals and other *ab initio* methods. In the future, with the proposed framework, it is promising to investigate a wide range of phenomena, including ferroelectricity, topological electronic transport, quantum Hall effect, and orbital magnetization, among others, on a higher level of accuracy and with electron correlations accounted for properly. Furthermore, this work provides more possibilities for utilizing neural network applications in condensed matter physics, especially when more efficient neural networks are developed.

The code of this work is publicly available from the open-source repository of DeepSolid [62].

This work is directed and supported by Hang Li and ByteDance Research. J. C. is supported by the National Natural Science Foundation of China under Grant No. 92165101.

*X. L. and Y. Q. contributed equally to this work.
†lixiang.62770689@bytedance.com
‡ji.chen@pku.edu.cn

[1] R. D. King-Smith and D. Vanderbilt, Theory of polarization of crystalline solids, Phys. Rev. B **47**, 1651 (1993).
[2] R. Resta, Macroscopic polarization in crystalline dielectrics: The geometric phase approach, Rev. Mod. Phys. **66**, 899 (1994).
[3] R. W. Nunes and X. Gonze, Berry-phase treatment of the homogeneous electric field perturbation in insulators, Phys. Rev. B **63**, 155107 (2001).
[4] I. Souza, J. Íñiguez, and D. Vanderbilt, First-principles approach to insulators in finite electric fields, Phys. Rev. Lett. **89**, 117602 (2002).
[5] B. Kirtman, V. Lacivita, R. Dovesi, and H. Reis, Electric field polarization in conventional density functional theory: From quasilinear to two-dimensional and three-dimensional extended systems, J. Chem. Phys. **135**, 154101 (2011).
[6] D. Xiao, M.-C. Chang, and Q. Niu, Berry phase effects on electronic properties, Rev. Mod. Phys. **82**, 1959 (2010).
[7] W. Kohn, Nobel lecture: Electronic structure of matter—wave functions and density functionals, Rev. Mod. Phys. **71**, 1253 (1999).
[8] M. van Faassen, P. L. de Boeij, R. van Leeuwen, J. A. Berger, and J. G. Snijders, Ultranonlocality in time-dependent current-density-functional theory: Application to conjugated polymers, Phys. Rev. Lett. **88**, 186401 (2002).
[9] B. Champagne, D. H. Mosley, M. Vračko, and J.-M. André, Electron-correlation effects on the static longitudinal polarizability of polymeric chains. II. Bond-length-alternation effects, Phys. Rev. A **52**, 1039 (1995).
[10] D. M. Ceperley and B. J. Alder, Ground state of the electron gas by a stochastic method, Phys. Rev. Lett. **45**, 566 (1980).
[11] W. M. C. Foulkes, L. Mitas, R. J. Needs, and G. Rajagopal, Quantum Monte Carlo simulations of solids, Rev. Mod. Phys. **73**, 33 (2001).
[12] G. H. Booth, A. Grüneis, G. Kresse, and A. Alavi, Towards an exact description of electronic wavefunctions in real solids, Nature (London) **493**, 365 (2013).
[13] P. Umari, A. J. Willamson, G. Galli, and N. Marzari, Dielectric response of periodic systems from quantum Monte Carlo calculations, Phys. Rev. Lett. **95**, 207602 (2005).
[14] P. Umari and N. Marzari, Linear and nonlinear susceptibilities from diffusion quantum Monte Carlo: Application to periodic hydrogen chains, J. Chem. Phys. **131**, 094104 (2009).

[15] G. Carleo and M. Troyer, Solving the quantum many-body problem with artificial neural networks, Science **355**, 602 (2017).
[16] Y. Nomura, A. S. Darmawan, Y. Yamaji, and M. Imada, Restricted Boltzmann machine learning for solving strongly correlated quantum systems, Phys. Rev. B **96**, 205152 (2017).
[17] G. Carleo, Y. Nomura, and M. Imada, Constructing exact representations of quantum many-body systems with deep neural networks, Nat. Commun. **9**, 1 (2018).
[18] J. Han, L. Zhang, and E. Weinan, Solving many-electron Schrödinger equation using deep neural networks, J. Comput. Phys. **399**, 108929 (2019).
[19] D. Pfau, J. S. Spencer, A. G. D. G. Matthews, and W. M. C. Foulkes, *Ab initio* solution of the many-electron Schrödinger equation with deep neural networks, Phys. Rev. Res. **2**, 033429 (2020).
[20] J. Hermann, Z. Schätzle, and F. Noé, Deep-neural-network solution of the electronic Schrödinger equation, Nat. Chem. **12**, 891 (2020).
[21] K. Choo, A. Mezzacapo, and G. Carleo, Fermionic neural-network states for *ab initio* electronic structure, Nat. Commun. **11**, 2368 (2020).
[22] M. Entwistle, Z. Schätzle, P. A. Erdman, J. Hermann, and F. Noé, Electronic excited states in deep variational Monte Carlo, Nat. Commun. **14**, 274 (2023).
[23] M. Scherbela, R. Reisenhofer, L. Gerard, P. Marquetand, and P. Grohs, Solving the electronic Schrödinger equation for multiple nuclear geometries with weight-sharing deep neural networks, Nat. Comput. Sci. **2**, 331 (2022).
[24] J. Hermann, J. Spencer, K. Choo, A. Mezzacapo, W. Foulkes, D. Pfau, G. Carleo, and F. Noé, *Ab initio* quantum chemistry with neural-network wavefunctions, Nat. Rev. Chem. **7**, 692 (2023).
[25] M. Wilson, S. Moroni, M. Holzmann, N. Gao, F. Wudarski, T. Vegge, and A. Bhowmik, Neural network ansatz for periodic wave functions and the homogeneous electron gas, Phys. Rev. B **107**, 235139 (2023).
[26] G. Cassella, H. Sutterud, S. Azadi, N. D. Drummond, D. Pfau, J. S. Spencer, and W. M. C. Foulkes, Discovering quantum phase transitions with fermionic neural networks, Phys. Rev. Lett. **130**, 036401 (2023).
[27] G. Pescia, J. Han, A. Lovato, J. Lu, and G. Carleo, Neural-network quantum states for periodic systems in continuous space, Phys. Rev. Res. **4**, 023138 (2022).
[28] X. Li, Z. Li, and J. Chen, *Ab initio* calculation of real solids via neural network ansatz, Nat. Commun. **13**, 7895 (2022).
[29] N. Yoshioka, W. Mizukami, and F. Nori, Solving quasiparticle band spectra of real solids using neural-network quantum states, Commun. Phys. **4**, 106 (2021).
[30] Y. Qian, W. Fu, W. Ren, and J. Chen, Interatomic force from neural network based variational quantum Monte Carlo, J. Chem. Phys. **157**, 164104 (2022).
[31] X. Li, C. Fan, W. Ren, and J. Chen, Fermionic neural network with effective core potential, Phys. Rev. Res. **4**, 013021 (2022).
[32] W. Ren, W. Fu, X. Wu, and J. Chen, Towards the ground state of molecules via diffusion Monte Carlo on neural networks, Nat. Commun. **14**, 1860 (2023).
[33] H. Xie, Z.-H. Li, H. Wang, L. Zhang, and L. Wang, A deep variational free energy approach to dense hydrogen, Phys. Rev. Lett. **131**, 126501 (2023).
[34] C. P. Robert and G. Casella, Controlling Monte Carlo Variance, in *Monte Carlo Statistical Methods*, Springer Texts in Statistics, edited by C. P. Robert and G. Casella (Springer, New York, 2004), pp. 123–156.
[35] R. W. Nunes and D. Vanderbilt, Real-space approach to calculation of electric polarization and dielectric constants, Phys. Rev. Lett. **73**, 712 (1994).
[36] R. Resta, Quantum-mechanical position operator in extended systems, Phys. Rev. Lett. **80**, 1800 (1998).
[37] See Supplemental Material at http://link.aps.org/supplemental/10.1103/PhysRevLett.132.176401 for additional theoretical discussion, computational details, and supporting data.
[38] J. Martens and R. Grosse, Optimizing neural networks with Kronecker-factored approximate curvature, in *International Conference on Machine Learning* (PMLR, 2015), pp. 2408–2417.
[39] E. Miliordos and K. L. C. Hunt, Dependence of the multipole moments, static polarizabilities, and static hyperpolarizabilities of the hydrogen molecule on the H–H separation in the ground singlet state, J. Chem. Phys. **149**, 234103 (2018).
[40] J. P. Harris, D. R. Manship, W. H. Breckenridge, and T. G. Wright, Comparison of the interactions in the rare gas hydride and group 2 metal hydride anions, J. Chem. Phys. **140**, 084304 (2014).
[41] N. E.-B. Kassimi and A. J. Thakkar, Static hyperpolarizability of atomic lithium, Phys. Rev. A **50**, 2948 (1994).
[42] D. Tunega, J. Noga, and W. Klopper, Basis set limit value for the static dipole polarizability of beryllium, Chem. Phys. Lett. **269**, 435 (1997).
[43] A. K. Das and A. J. Thakkar, Static response properties of second-period atoms: Coupled cluster calculations, J. Phys. B **31**, 2215 (1998).
[44] Q. Sun, T. C. Berkelbach, N. S. Blunt, G. H. Booth, S. Guo, Z. Li, J. Liu, J. D. McClain, E. R. Sayfutyarova, S. Sharma *et al.*, PySCF: The PYTHON-based simulations of chemistry framework, Wiley Interdiscip. Rev. **8**, e1340 (2018).
[45] P. Schwerdtfeger and J. K. Nagle, 2018 table of static dipole polarizabilities of the neutral elements in the periodic table, Mol. Phys. **117**, 1200 (2019).
[46] A. Annaberdiyev, C. A. Melton, M. C. Bennett, G. Wang, and L. Mitas, Accurate atomic correlation and total energies for correlation consistent effective core potentials, J. Chem. Theory Comput. **16**, 1482 (2020).
[47] G. Kresse and J. Hafner, Norm-conserving and ultrasoft pseudopotentials for first-row and transition elements, J. Phys. Condens. Matter **6**, 8245 (1994).
[48] G. Kresse and J. Furthmüller, Efficient iterative schemes for *ab initio* total-energy calculations using a plane-wave basis set, Phys. Rev. B **54**, 11169 (1996).
[49] M. A. Watson, P. Sałek, P. Macak, and T. Helgaker, Linear-scaling formation of Kohn-Sham Hamiltonian: Application to the calculation of excitation energies and polarizabilities of large molecular systems, J. Chem. Phys. **121**, 2915 (2004).

[50] E. F. Archibong and A. J. Thakkar, Chain length dependence of static longitudinal polarizabilities and hyperpolarizabilities in linear polyynes, J. Chem. Phys. **98**, 8324 (1993).
[51] E. K. Dalskov, J. Oddershede, and D. M. Bishop, Static and dynamic polarizability calculations for the polyyne series ($C_{2n}H_2$) with extrapolation to the infinite chain, J. Chem. Phys. **108**, 2152 (1998).
[52] N. Rusman and M. Dahari, A review on the current progress of metal hydrides material for solid-state hydrogen storage applications, Int. J. Hydrogen Energy **41**, 12108 (2016).
[53] M. Burkatzki, C. Filippi, and M. Dolg, Energy-consistent pseudopotentials for quantum Monte Carlo calculations, J. Chem. Phys. **126** (2007).
[54] J. P. Perdew, K. Burke, and M. Ernzerhof, Generalized gradient approximation made simple, Phys. Rev. Lett. **77**, 3865 (1996).
[55] G. Barrera, D. Colognesi, P. Mitchell, and A. Ramirez-Cuesta, LDA or GGA? A combined experimental inelastic neutron scattering and *ab initio* lattice dynamics study of alkali metal hydrides, Chem. Phys. **317**, 119 (2005), combining simulations and neutron scattering experiments: From models to systems of biological and technological interest.
[56] E. Staritzky and D. I. Walker, Crystallographic data. 124. lithium hydride, LiH; 125. lithium deuteride, LiD, Anal. Chem. **28**, 1055 (1956).
[57] K. Ghandehari, H. Luo, A. L. Ruoff, S. S. Trail, and F. J. DiSalvo, Band gap and index of refraction of CsH to 251 GPa, Solid State Commun. **95**, 385 (1995).
[58] S. S. Batsanov, E. D. Ruchkin, and I. A. Poroshina, *Refractive Indices of Solids* (Springer, New York, 2016).
[59] E. K. Yu, D. A. Stewart, and S. Tiwari, *Ab initio* study of polarizability and induced charge densities in multilayer graphene films, Phys. Rev. B **77**, 195406 (2008).
[60] S. Slizovskiy, A. Garcia-Ruiz, A. I. Berdyugin, N. Xin, T. Taniguchi, K. Watanabe, A. K. Geim, N. D. Drummond, and V. I. Fal'ko, Out-of-plane dielectric susceptibility of graphene in twistronic and Bernal bilayers, Nano Lett. **21**, 6678 (2021).
[61] A. Laturia, M. L. Van de Put, and W. G. Vandenberghe, Dielectric properties of hexagonal boron nitride and transition metal dichalcogenides: From monolayer to bulk, npj 2D Mater. Appl. **2**, 6 (2018).
[62] X. Li, bytedance/deepsolid: Release 1.0 (2022), 10.5281/zenodo.7385395.